Three-dimensional modeling of resonant charge transfer between ion beams and metallic surfaces

I. K. Gainullin*

Faculty of Physics, Moscow State University, Leninskie gory 1 #2, Moscow 119992, Russia

(Received 4 March 2017; revised manuscript received 6 April 2017; published 17 May 2017)

This study addresses the numerical modeling of resonant charge transfer (RCT) during ion-surface interactions. In our approach we use the original *ab initio* three-dimensional (3D) time-dependent Schrödinger equation solver in combination with 3D pseudopotentials, which describe the metal structure on the atomic level. Full 3D modeling enables us to reveal such fundamental RCT aspects as anisotropy of electron propagation in the target and electron delay during grazing scattering. We have also refined the theoretical basis for RCT experiments calculations and achieved quantitative correspondence to a large variety of experimental data.

DOI: 10.1103/PhysRevA.95.052705

I. INTRODUCTION

The investigation of resonant charge transfer (RCT), i.e., energy-conserving one-electron tunneling through the potential barrier between an atomic particle and a surface, is of fundamental and practical importance in several branches of physics and chemistry [1–3]. Note that in most cases RCT is the dominant channel of electron exchange between an atomic particle and bulk metal [4].

The problem of RCT between an atomic particle and bulk metal has been intensively explored during the last two decades. Among many interesting scientific results we should mention are (i) RCT dependence on ion-surface distance, and energy of the ion beam and scattering angle [5–8]; (ii) nonadiabatic effects [5,9]; (iii) parallel velocity effect during grazing scattering [3,4,10–14]; (iv) quantum-size effect for RCT with nanosystems [15–22]; (v) RCT dependence on surface structure (atomic structure, adsorbates, corrugations, etc.) [23–29]. Also, a lot of experimental data has been accumulated. In most studies the systems with one active electron, such as H^- and metal surface or Li^0 and metal surface are concerned. This choice is stipulated not only by simplicity of numerical description, but because the above atomic particles allow one to investigate RCT more efficiently. The reason is that the H^- affinity level (–0.75 eV from vacuum) is located above, and alkali-metal ionization energy (e.g., –5.4 eV for Li) is located very close to the Fermi energy of many metals (from –4 to –5.5 eV). Note that affinity and ionization levels also depend on ion-surface distance; e.g., near the surface hydrogen's affinity level decreases down to –10 –15 eV. Hence the electron transfer between the H^- alkali-metal ion and typical metal could be realized in two directions (electron loss from atomic particle to metal and electron capture by atomic particle). This condition is not realized for numerous other atomic particles, e.g., the simplest H^+ ion with energy level –13.6 eV. Hereby H^- and Li^0/Li^+ are good prototypes for investigation of electron loss and electron capture processes. There are a number of experimental studies, where RCT with more complicated ions, such as O^0/O^-, F^0/F^-, or Ar^+/Ar^0, exhibits the same regularities as RCT with prototype ions [4,30].

The widely used approach to RCT modeling is the calculation of electron loss or capture on the outgoing trajectory after ion-level intersection with the Fermi level of the metal. A detailed review of RCT modeling is given in Ref. [4]. The typical RCT problem requires numerical modeling of the three-dimensional (3D) spatial domain, about 10^3–10^4 nm^3, that corresponds to the numerical grid, about 10^9–10^{10} points [31,32]. The numerical simulation of such volumes is very resource consuming, thus initially many studies have exploited different dimension reduction (1D and 2D) techniques, such as complex angular mode and wave-packet propagation [12,17,18,21,33]. Thus, for the calculation of electron transfer probability in real 3D experiments, the rate equation is used [5,7,25], which implies that the electron transfer rate depends only on the ion-surface distance, but not on the ion velocity (adiabatic approximation). There are also approaches when a 2D "X-Z" coordinate system is used and obtained results are multiplied by some "3D factor" [24]. For the grazing trajectories an additional translational factor and model of "shifted Fermi spheres" are applied [4,10,34]. In some cases such approaches give reasonable correspondence to experimental data [3,5,11,30], but they could not account for nonadiabatic effects in 3D geometry and the atomic structure of the surface. For example, in Refs. [3,7,30] the H^- fraction depends on ion beam orientation relative to the Cu(110) surface lattice; such azimuthal dependence could not be distinguished by the existing theory. In some studies the 3D experiments [6] were compared only with calculation results for the "jellium" model (adiabatic approximation). In some studies the calculations give only qualitative correspondence to experimental data [8].

Due to the limitations of 1D and 2D techniques, the metal surface (bulk) cannot be modeled by fair 3D pseudopotential with periodicity on X, Y, and Z coordinates. Instead of this, two types of 1D pseudopotentials (dependent on Z only) are widely used. The first type is used for description of jelliumlike metals [35], the second for the modeling of metals with projected band gap [36]. Despite their simplicity, these pseudopotentials successfully reproduce some RCT features. In recent years the 2D pseudopotential for Cu(110) was presented [37].

The first time the 3D RCT calculations were mentioned in 2000 [38], the reported system size (10^7 points) was too small to solve real 3D RCT problems. Also, 3D calculations were reported in 2005 and 2009, but their details and complexity are omitted [8,26]. In recent years the 3D RCT calculations were presented, which are based on numerical solving of the time-dependent Schrödinger equation (TDSE) with the

*ivan.gainullin@physics.msu.ru

Anderson-Newns Hamiltonian [28,29]. They take into account the atomic structure of the surface and show correspondence to some experimental data, but the question of correct (*ab initio*) accounting of the electron kinematic factor is not clear. Note that these calculations show RCT azimuthal dependence, but direct comparison to "azimuthal-dependent" experimental data is not given.

In 2015 we introduced the 3D GPU (graphical processing units) TDSE solver [31,32] and applied it to RCT modeling in nanosystems [22]. The key advantage of the GPU TDSE solver is direct TDSE solution for large spatial domains (up to 10^5 nm^3). It was achieved due to the effective parallelization of a simple, explicit numerical scheme on GPUs. In this paper we combine the direct 3D calculations with *ab initio* 3D pseudopotentials for surface description (obtained by means of Density Functional Theory (DFT)). The presented technique enables direct RCT modeling, accounting for surface structure. Also, we present refinement of theoretical basic and calculation methodology for three-dimensional RCT modeling. As a next step we apply them to a wide set of RCT experiments, covering various RCT aspects, and good quantitative correspondence was obtained. In Sec. II the theoretical basis of RCT calculation is introduced. Section III is devoted to 3D RCT effects. In Sec. IV we discuss the results of 3D calculations for various RCT experiments. Section V contains some concluding remarks.

For convenience the atomic system of units (with $m_e = e = \hbar = 1$; 1 a.u. of distance is equal to 0.53 Å, 1 a.u. of time is equal to 2.419×10^{-17} s, and 1 a.u. of velocity is equal to 2.188×10^8 cm/s) is used in this article (if not clearly stated otherwise).

II. THEORETICAL BASIS OF RCT CALCULATION

A. Numerical method

The typical RCT problem during ion-surface interaction includes (i) an atomic particle; (ii) the surface; (iii) an electron moving in the pseudopotential of the ion and the surface. The RCT calculation is based on the numerical solution of the TDSE. In this research we use an original high-performance *ab initio* 3D numerical TDSE solver which utilizes graphical processing units. The details about the TDSE solver parallel implementation, verification, performance, and scalability are given in Refs. [31,32]. At a glance, we consider TDSE in the form

$$i\frac{d\psi(\vec{r},t)}{dt} = \left[-\frac{\Delta}{2} + U(\vec{r},t)\right]\psi(\vec{r},t), \qquad (1)$$

where $U(\vec{r},t) = V_{\text{ion}}(\vec{r},t) + V_{e\text{-surf}}(\vec{r})$ is the time-dependent potential.

To find z_f (the distance, where the atomic energy level intersects the Fermi level), one has to know the atomic particle (ion) energy level as a function of the ion-surface distance. In the first approximation it depends on distance as $E(z) = E(\infty) \pm 1/4z$ for positive and negative ions respectively. But for more complicated case, e.g. surfaces with projected band gap or adsorbates, $E(z)$ can deviates from the above simple law (e.g. split due to the avoided crossing [26,33]). Hence $E(z)$ should be defined numerically. To do this, one has to solve a set of "static" problems, for different fixed ion-surface distances. Then, knowing the autocorrelation function for a certain ion-surface distance, one can find the atomic particle energy level [22]. The RCT rate calculation is discussed in Sec. II C.

Equation (1) requires pseudopotentials for the atomic particle and the metal surface. For the ions under study (H^0/H^-, Li^0/Li^+, Na^+, K^+), the analytical pseudopotentials are available [39,40]. For example, the pseudopotential for the H^- ion is chosen as $V_{H^-}(r) = -(1 + 1/r)\exp(-2r) - (\alpha_H/r^4)\exp(-r_0^2/r^2)$($r$ is the radial electron-atom distance in atomic units, $\alpha_H = 2.25$ and $r_0^2 = 2.547$) [39,41]. In this study we use 3D pseudopotentials for Cu(100), Cu(110), and Cu(111) surfaces, which are obtained by means of DFT calculations (see Sec. II B for details). Copper crystal is a very common choice for the RCT modeling and experimental measurements. Moreover, the Cu(110) surface on one side and Cu(100) and Cu(111) surfaces on the other represent the free-electron surface and the surface with a projected band gap, respectively. In other cases, when the atomic structure of the surface is not important, we use 1D analytical pseudopotentials for RCT calculation [35,36].

Note that for modeling of a moving hydrogen anion the electron translation factor (ETF) should be applied, which results in multiplication of the initial electron wave function on $\text{ETF} = \exp(-i\vec{v}\otimes\vec{r})$ [28].

B. Pseudopotentials calculation

For DFT calculation of the metal's electronic structure we use a supercell technique (QUANTUM ESPRESSO [42], VASP [43]). For each surface two series of calculations were done: (i) "surface" calculations; (ii) "volume" calculations. The surface calculations were performed for the slab of 7 monolayers thickness in a supercell of 14 monolayers thickness. The volume calculations were done in the supercell of 1 monolayer thickness, but the width and length of the supercell were chosen equal to the surface calculations. This leads to a redundant number of atoms for volume calculations, but enables easy pseudopotential replication along the surface normal onto the semi-infinite 3D TDSE domain.

The DFT calculations were done in the plane-wave basis, with local-density approximation for exchange-correlation potential. The integration over the Brillouin zone was performed using the tetrahedron method with Blöchl corrections. The Brillouin zone was sampled using $11 \times 11 \times 11$ k-point mesh in a Monkhorst-Pack grid. A cutoff energy of 1000 eV was used. According to our measurements, the total energy converges under the above parameters. The one-electron pseudopotential was obtained as a sum of ionic core potential, electron repulsion potential, and exchange-correlation potential (see [28,29] for details).

In our calculations we used fixed fcc copper crystallographic structure without surface relaxation or reconstruction. Also, the DFT calculations were done for an isolated copper surface, without an adjacent hydrogen atom. One could note that for "full *ab initio* RCT calculations" we have to calculate the pseudopotential for a metal surface, perturbed by the ion. However, such an approach is not viable for direct TDSE solution, because the DFT calculations should be performed for each point of the ion trajectory. Instead of this we use the approach of the full pseudopotential for RCT calculations being a superposition of the surface pseudopotential and the

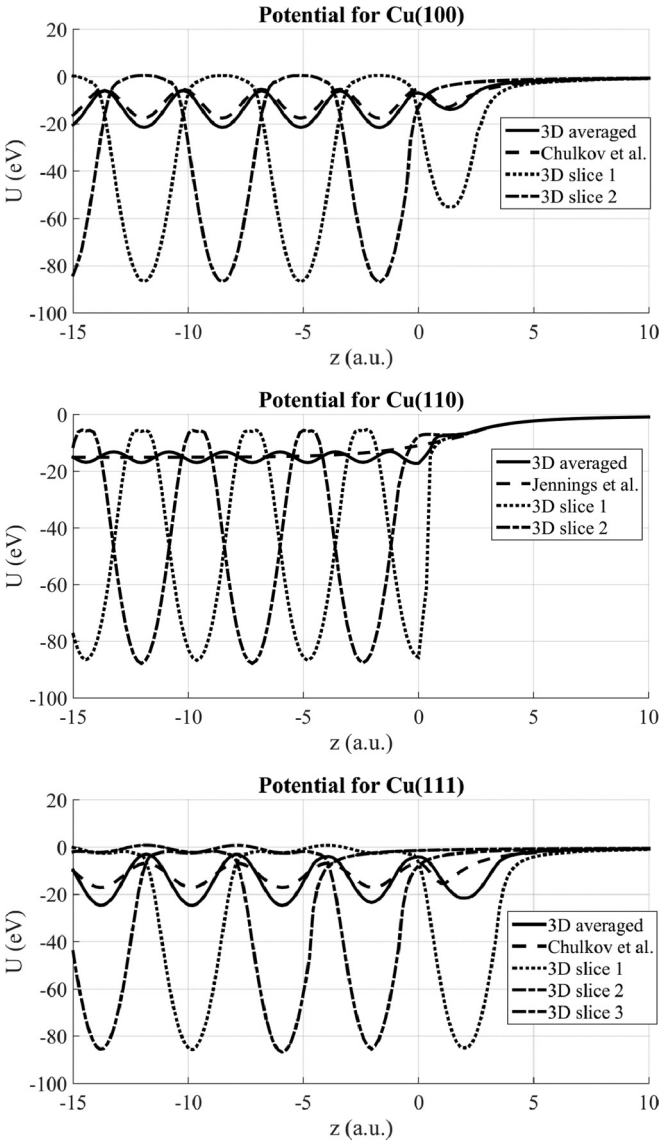

FIG. 1. Cu(100), Cu(110), and Cu(111) pseudoponetial dependence on the Z coordinate. One-dimensional pseudopotentials referred to as "Jennings *et al.*" and "Chulkov *et al.*" are taken from Refs. [35,36], respectively.

potential of the ionic core. Therefore in the vacuum region the obtained zero potential should be replaced by an image charge potential such as the pseudopotentials in Refs. [35,36]. For ion-surface distances greater than 3 a.u. such approach is reasonable and commonly used for RCT calculations [4]. Note that in most practical calculation RCT is considered for ion-surface distances greater than 6–9 a.u., where the ion charge state formation occurs.

A reasonable question is the comparison of obtained 3D pseudopotentials for Cu(100), Cu(110), and Cu(111) with 1D pseudopotentials [35,36], that were verified in manystudies. Figure 1 shows the averaged 3D pseudopotential, its slices along special lines, and the corresponding 1D potential. We see that the averaged 3D potentials correspond well with the 1D potentials. In order to reproduce the potential in the vacuum region for Cu(100) and Cu(111) the surface layer was "shifted"

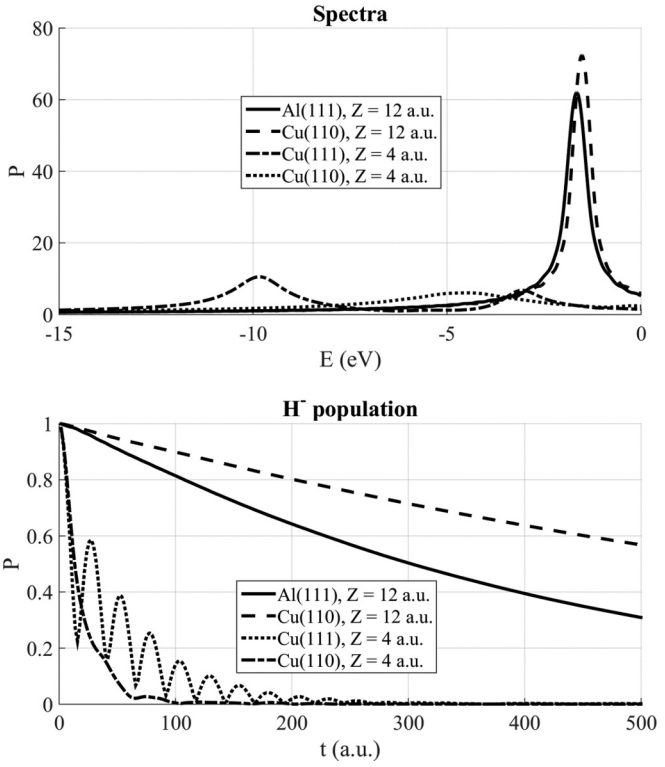

FIG. 2. Comparison of electron decay for H^- fixed at distance Z in front of different surfaces (see legend for details). Upper figure shows the energy spectra, lower, the dependence of H^- occupation on time.

into the vacuum and its potential well was decreased to fit the image charge potential. Note that distances between the first and second atomic layers for 3D potentials differ from those for 1D potentials, because we have used a "clear" crystallographic structure without reconstruction and relaxation.

C. Level width and RCT rate calculation

The RCT rate (i.e., the amount of transferred electron density per unit of time) calculation is rather important, e.g., for usage in the rate equation (RE). In theory, the RCT rate is determined by the width of ion state resonance [8,25,26,44]. However, model calculations show that for RCT rate determination it is more robust to calculate it as the decay rate of the autocorrelation function modulus (see Ref. [4] for details). In Fig. 2 level widths and RCT rates for different systems are compared. For example, the level width for the H^- ion located in front of the Al(111) and Cu(110) surfaces is approximately the same, but the RCT rate differs twice. In the presented case, for both surfaces we have the exponential decay of the ionic state. Note that the RCT rate (decay constant) practically does not change in time.

A special case is RCT with projected band-gap surfaces, when ion occupation exhibits oscillations. For example, Fig. 2 shows energy spectra and occupation for the H^- ion located in front of the Cu(111) and Cu(110) surfaces. We see that the decay rates at the initial time moment are similar for both surfaces, while the width of the energy levels differs significantly. The decay rate for Cu(111)

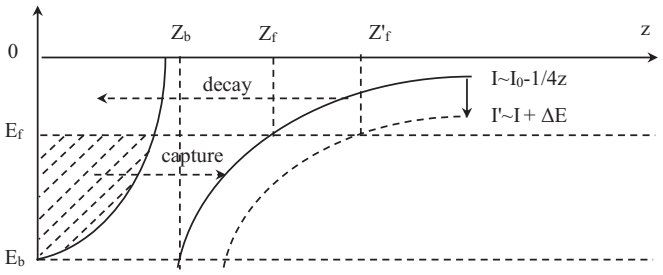

FIG. 3. Illustration of main RCT aspects (details are given in the text).

obviously depends on time and even changes sign. Therefore we use only the initial part of the autocorrelation function (until the first minimum), to calculate the RCT rate for the RE.

D. Physical model of RCT experiments calculation

Figure 3 illustrates the main theoretical points of RCT between static atomic particles (ions or neutral atoms) and metallic targets:

(1) In metal electrons energies correspond to Fermi-Dirac distribution. This means that for room-temperature conditions all electronic states below Fermi energy (Fermi level) are occupied, while all electronic states above Fermi energy are vacant. Therefore if the energy level of the atomic particle is located above Fermi energy the only electron loss by the atomic particle is allowed, and vice versa only electron capture is possible for atomic particles, located below Fermi energy.

(2) Due to the interaction with image charge, the ion energy level depends on the ion-surface distance [4]. Approximate dependence is $E(z_{\text{ion-surface}}) = E(\infty) + 1/4z$ for positive ions and $E(z_{\text{ion-surface}}) = E(\infty) - 1/4z$ for negative ions. Hence the energetically allowed electron transfer direction (electron loss or electron capture) depends on ion-surface distance. In the first approximation the RCT direction switches (loss to capture or vice versa) at the distance z_f, where the ion energy level crosses the Fermi level of the metallic target.

In the case of moving atomic particles we have to take into account the following:

(3) The final charge state of the atomic particle (ion occupation or population) is formed on the outgoing part of the trajectory. This happens because near the surface ($z \sim$ 1–3 a.u.), the ion-surface interaction is so strong that the charge state of the atomic particle reaches its equilibrium that does not depend on initial conditions (so-called "memory loss" effect). This suggestion is supported by several experimental studies [7,9,11,12,45], where the final fraction of scattered H^- and Li^+ ions does not depend on the primary ion beam charge state (negative or positive ions) and incidence angle. Moreover, the final ion charge state formation occurs at ion-surface distances about 6–9 a.u. [4]. For example, for the rate equation calculations the final charge state does not depend on the selected initial charge state [3,30].

(4) The interaction with the image charge influences the atomic particle trajectory, but the benefit from the usage of realistic trajectories is limited to 10% [11,24,27]. Hence in our calculation we use classical trajectories; i.e., the atomic particle is moving along a straight line with constant velocity.

(5) Galilean transformation from the rest frame of the target to the frame of the moving atomic particle blurs the effective electron energy distribution in metal. As a result the electrons in metal conform to Doppler-Fermi-Dirac distribution [4,34]. Therefore for moving particles concurrent processes of electron loss and electron capture are possible at the same time.

(6) In the case of Galilean transformation from the ion's frame to the target's frame, the wave vector of the ion's electron is summed with its velocity. The ion's energy level in this case is shifted. In some studies [4,46] the shift of the energy level is given as $+v^2/2$, but this is correct only for the case when the wave vector is orthogonal to the ion's velocity $\vec{v}$ (e.g., grazing scattering).

Our approach to RCT calculation is based on the above statements. The key point of the RCT physical model is determination of energetically allowed electron transfer direction (electron loss or electron capture).

(7) We perform RCT direction analysis in k space, since this is more informative compared to a simple energy level comparison. Active electron distribution inside the metal in k space is obtained by Fourier transform of the electron's wave function $f(\vec{k}, t) = \frac{1}{2\pi}\int_{z<0} d\vec{r}^3 \psi(\vec{r}, t)\exp(-i\vec{k}\cdot\vec{r})$. Note that in the case of cylindrical symmetry (e.g., the 2D wave-packet propagation method in z-ρ coordinates), the zero-order Hankel transform should be applied for the radial coordinate instead of the Fourier transform.

Figure 4 shows the electron distribution in k space for some simple systems: (i) H^- near the Cu(110) surface and (ii) Li^0 near the Ag(111) surface. Despite RCT being a dynamical process, for most ion-surface systems the electron distribution becomes stationary after a short time of interaction (50–100 a.u.). We see that in the first case (free-electron surface) the electron is tunneling inside the metal along the surface normal. In the second case (surface with projected band gap), the electron propagates mainly parallel to the surface. Note that the presented distributions have a simple form and a dominant wave vector value $\vec{k}$ can be determined. The quantity $|\vec{k}|^2/2$ corresponds to the ion energy level measured from the conduction band bottom of the target.

Since we perform *ab initio* 3D RCT modeling with surface description on the atomic level, the calculations are produced in the target's frame, so the above shown $f(\vec{k})$ distributions should be transferred to the target's frame: $f(\vec{k}' = \vec{k} + \vec{v}) = f(\vec{k})$, where $\vec{v}$ is ion velocity (see inset in Fig. 4).

(8) In the case of simple $f(\vec{k})$ distributions (single point in k space) and relatively small ion velocities (<0.3 a.u.), i.e., when $f(\vec{k})$ distribution does not change significantly, we directly solve the TDSE to calculate one-way RCT (e.g., electron loss by H^- or electron capture by Li^+) on the part of the outgoing trajectory $z > z_f$; z_f is calculated from the equation $E_f = I(z_f) + \Delta E(z_f)$, where the ion-level energy shift is calculated as $\Delta E(z_{\text{ion-surface}}) = |k'|^2/2 - |k|^2/2 = |v|^2/2 - \vec{v}\cdot\vec{k}$. The initial charge state of the atomic particle $P_0 = P(z_f)$ is a fitting parameter or can be calculated by means of the rate equation. The details of theTDSE numerical solution are given in Sec. II A.

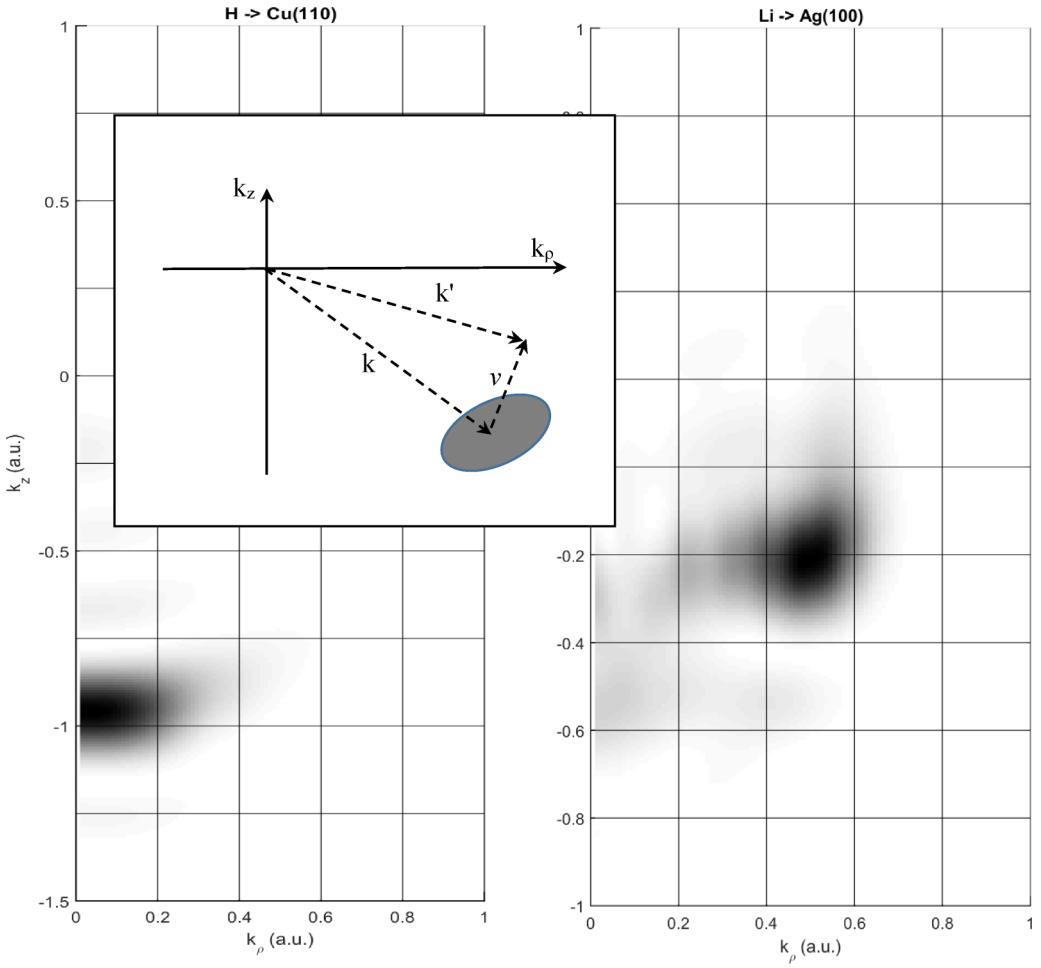

FIG. 4. Ions' outer electron density distribution in 2D k space inside the target. Left: H^- near Cu(110) surface. Right: Li^0 near Ag(111) surface. Ion-surface distance is 7 a.u., interaction time is 100 a.u. Inset illustrates frame transformation (details are given in the text).

(9) In the case of complex $f(\vec{k})$ distributions or significant ion velocities, e.g., experiments on the parallel velocity effect during grazing scattering, concurrent electron loss and capture processes should be taken into account. In this case our calculation technique is very close to Refs. [3,9,12,14,30]. The significant advantage is that we use 3D $f(\vec{k})$ distributions, which enables us to model 3D effects, including RCT azimuthal dependence. The technique is based on rate equation integration. For example, occupation of the negative ion is calculated from the following equation:

$$\frac{dP^-}{dt} = -\Gamma_{\text{loss}} P^- + \Gamma_{\text{capture}}(1 - P^-), \tag{2}$$

where $\Gamma_{\text{loss}}(z) = g_{\text{loss}}\Gamma(z)F_{\text{loss}}$, $\Gamma_{\text{capture}}(z) = g_{\text{capture}}\Gamma(z)F_{\text{capture}}$, and $\Gamma(z)$ is the RCT rate (see Sec. II C for details of its calculations).

The statistical factors $g_{\text{capture}}, g_{\text{loss}}$ are equal to 1 and 0.5 for the hydrogen anion. Weights for electron loss and capture probabilities are proportional to the part of the electron density located outside and inside the Fermi sphere, respectively:

$$F_{\text{loss}} = \int_{|\vec{k}'|>k_f} d\vec{k}'^3 |f(\vec{k}')|^2, \quad F_{\text{capture}} = \int_{|\vec{k}'|<k_f} d\vec{k}'^3 |f(\vec{k}')|^2. \tag{3}$$

Note that for small normal velocities, as in grazing scattering collisions, the adiabatic approximation is viable and RE gives very good results [3,9,12,30]. Moreover in this case the charge state is formed on the distances $z = 6$–9 a.u. [4,9,12], so the final ion occupation does not depend on the initial chare state, e.g., $P_0(z = 3\,\text{a.u.})$ [12]. This means that the presented RCT calculation model is parameter free, but is limited to adiabatic conditions.

E. Adiabatic approximation and influence of ion velocity

It is known that adiabatic approximation is not appropriate for the RCT description with projected band-gap surfaces [5]. The main reason is that it does not take into account the electron reflection and its tunneling back to the ion in the case of interaction with projected band-gap surfaces. The only exception is the case of short interaction time (ion velocity $\sim$1 a.u.). Another important case of adiabatic approximation (rate equation) usage is RCT calculation during grazing scattering, that is characterized by small normal velocities ($\sim$0.02 a.u.) and long interaction times. RE gives satisfactory results not only for jellium surfaces such as Cu(110) or Al(111) [3,11,30], but for the surfaces with a projected band gap, e.g., Cu(111) [3,4,30]. A possible reason for successful RE application to RCT during grazing scattering

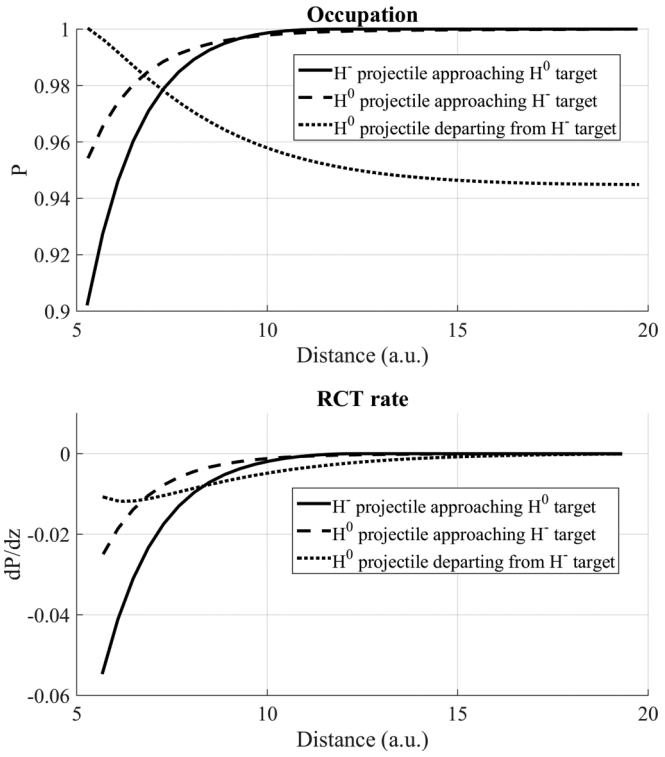

FIG. 5. Ion-level occupation (population) and decay rate for different systems (see legend for details). The projectile velocity is 0.2 a.u. (1 keV).

of H^- on projected band-gap surfaces is the so-called "electron delay" effect (see Sec. III B). If the target is described by an *ab initio* 3D pseudopotential—the electron propagation velocity in the target is less compared to the velocity of the moving ion. As a result, at each moment of time the H^- ion "sees" the "clear surface" (without a tunneled electron); hence the nonadiabatic effects caused by a projected band gap are eliminated.

In this section we further investigate the influence of ion velocity on the adiabatic approximation applicability to the RCT problem modeling. The system, consisting of a neutral hydrogen atom and hydrogen anion was selected as the model. Note that in the selected model we consider RCT between two hydrogen atoms; one of them is treated as a "projectile" and the other as a "target." Since the above system has one active electron, both "electron loss by projectile" and "electron capture by projectile" processes can be modeled directly, contrary to RCT between an ion and a metallic surface.

The velocity of the projectile was chosen as 0.2 a.u. (equal to energy of 1 keV). Figure 5 represents different collision cases: (i) the H^- projectile approaching the H^0 target; (ii) the H^0 projectile approaching the H^- target; (iii) the H^0 projectile departing from the H^- target.

Comparison of the H^- projectile approaching the H^0 target and the H^0 projectile approaching the H^- target shows that ion velocity affects the RCT rate; the ion state decays more rapidly in the case of an ion moving toward the target. Hence the major problem of widely used adiabatic approximation is the lack of projectile velocity influence. Note that adiabatic approximation becomes viable for smaller velocities (0.02 a.u.).

The comparison of the H^- projectile approaching the H^0 target and the H^0 projectile departing from the H^- target cases addresses the so-called "time-reversal symmetry" which assumes that electron capture by the departing atom is equivalent to electron loss by the approaching ion. One can see that this approximation is not correct. The RCT rate, as well as the final ion population, differs significantly for both cases. The surprising fact is that the time-reversal symmetry approach gives quantitative correspondence for some experiments on RCT between the Ag surface and Li atom [5,32].

III. THREE-DIMENSIONAL EFFECTS OF RESONANT CHARGE TRANSFER

In this section we describe the features arisen from the full 3D modeling of the RCT process. In Sec. III A we show the common picture of RCT with 3D pseudopotentials and compare the main numerical RCT characteristics to the case of widely used 1D pseudopotentials. Is Sec. III B we describe the electron delay effect, which is extremely important in the case of grazing scattering. In Sec. III C the anisotropy of electron propagation and its influence on RCT azimuthal dependence are discussed.

It should be mentioned that in the beginning of this research we expected to observe the RCT dependence on the ion beam orientation relative to 3D crystallographic axes, e.g., greater RCT rates for the ion approaching the surface along the direction of dense atomic packing (by analogy of Vener spots). But such suggestion was not supported by numerical simulations.

A. 3D RCT illustration and influence of ion lateral position

Figure 6 shows the time evolution of electron density for Cu(100) and Cu(110) surfaces for a fixed ion-surface distance. We see that for both surfaces electron distribution inside the metal reproduces its atomic structure; e.g., the central inset shows that for Cu(110) several surface atoms are populated during the first RCT moments. During the first RCT stage the electron distributions inside both surfaces are similar. Significant structural difference is observed on later stages—for the free-electron Cu(110) surface the electron propagates deep into the metal, while for Cu(100) with a projected band-gap the electron is distributed within several surface layers. On the qualitative level it corresponds to existing experimental and theoretical knowledge.

The hydrogen ion survival probability for the 3D pseudopotential demonstrates quantitative correspondence to the 1D potentials results (Fig. 7, upper part). For a free-electron Cu(110) surface the linear ion state decay occurs, while for Cu(100) the ion population exhibits oscillations near the 90% level. The explanation of such difference is rather simple: For Cu(110) the interlayer distance is 2.55 Å, while for Cu(100) it is 3.61 Å. Therefore in the first case the eigen-wave-function of adjacent atoms overlaps enough for the electron transport, while in the second case the electron transport is blocked in a certain energy interval. A qualitative difference for Cu(110) was observed for the small ion-surface distances (∼5 a.u.):

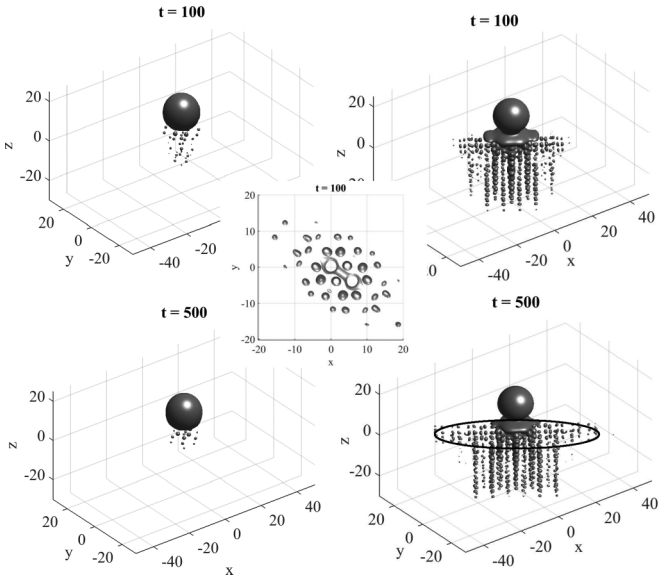

FIG. 6. Evolution of electron density for Cu(100), left side, and Cu(110), right side. Ion-surface distance is 12 a.u. Figure shows isosurfaces of electron density at sequential time moments (see figure for details). The inset in the center shows electron density distribution in the first surface layer of Cu(110).

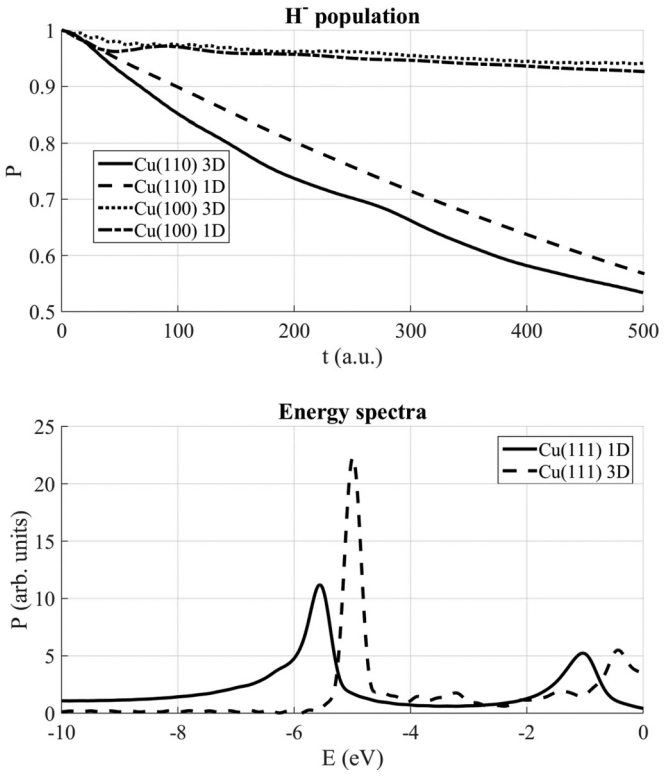

FIG. 7. Upper: comparison of hydrogen anion decay for different pseudopotentials and surfaces (see legend for details). The figure shows H^- ion population as a function of time. Ion-surface distance is 12 a.u. Lower: surface state energy comparison for 1D and 3D pseudopotentials (see legend for details). Ion-surface distance is 47 a.u.

The population calculated by means of the 1D potential shows exponential decay, while it was found to oscillate in the case of the 3D pseudopotential. This difference has an objective character, because the 3D potential reproduces real atomic structure of the surface, while the 1D potential for Cu(110) is flat inside the metal. For larger ion-surface distances this difference is not significant, because of the higher RCT electron energy.

Another reasonable 3D pseudopotential verification is surface state resonance, which takes place for surfaces with a projected band gap. Figure 7 (lower) shows a comparison of energy spectra, obtained with 1D and 3D pseudopotentials for Cu(111). We see that the 1D pseudopotential better reproduces the energy of the surface state for Cu(111) equal to –5.33 eV. Note that in 1D potentials the distance between the first and second layers differs from the interlayer distance in the bulk (see Fig. 1). This difference numerically affects the position of the surface state resonance. At the same time for the 3D pseudopotential we use a clear crystallographic structure with constant interlayer distance. An interesting fact is that simple relaxation of the top surface layer in 3D pseudopotential calculation does not lead to more precise surface energy value. Probably more complicated surface reconstruction is necessary. This is an obvious way for the 3D pseudopotentials' improvement.

The dependences of ion-level position and average decay rate (level width) on ion-surface distance also show good correspondence between 1D and 3D pseudopotentials.

Hereby we can conclude that the presented 3D pseudopotentials demonstrate qualitative resemblance with their 1D counterparts and they could be used for model calculations as well as for experiment modeling. Developed 3D potentials for Cu have given quantitative correspondence to the experimental data (see Sec. IV).

The ion's lateral position was found to have a small influence on the RCT rate and character. For a static problem, when the ion is fixed in front of a metal surface, the difference of RCT rates for various ions' lateral position is less than 5% when the ion-surface distance is 12 a.u., and is about 10% when the ion-surface distance is 5 a.u. Note that for the dynamic problem, when the ion is impinging on the surface or is moving away from the surface, the influence of the ion's lateral position (position of point of closest approach) was not detected (except in the case of close to normal collisions). This happens due to ion interactions with several adjacent surface atoms and this interaction is averaging due to the ion movement parallel to the surface.

B. Electron delay effect

An interesting 3D effect arises for the dynamical problem, when the ion has a velocity component parallel to the surface. In the case of the 1D pseudopotential (has a constant value in XY plane) the electron tunneled into the metal preserves the lateral velocity component, but for the real 3D pseudopotential electron movement parallel to the surface is limited due to the pseudopotential periodicity. Therefore the electron in the metal is delayed compared to the moving ion (Fig. 8, upper). This fact has a very interesting consequence for the surfaces with a projected band gap. For example, in Fig. 8 (lower) occupation of the H^- ion moving away from the Cu(111) surface

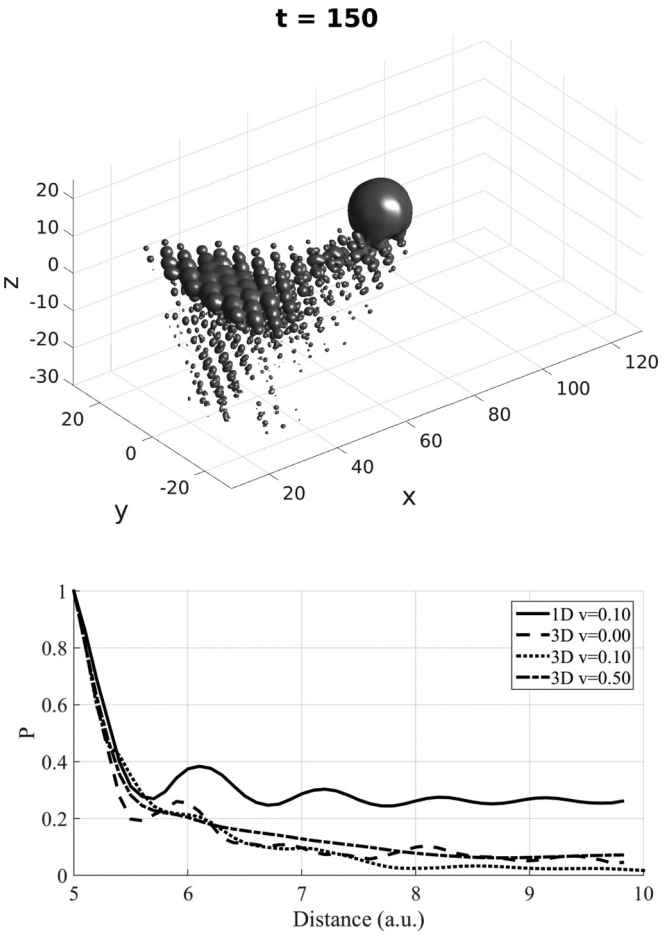

FIG. 8. Illustration of electron delay effect with 3D pseudopotential usage. Upper, electron density distribution at $t = 150$ a.u. for 3D pseudopotential. Lower: H^- population as a function of distance from the surface for 3D and 1D pseudopotentials. The H^- ion moves away from the Cu(111) surface with $V_{norm} = 0.02$ a.u.; initial ion-surface distance is 5 a.u. For the upper picture $V_{par} = 0.5$ a.u.; for the lower picture calculations with different V_{par} are presented (see "v" value in legend). The outgoing trajectory was chosen because it is often used for RCT experiments calculations.

exhibits oscillations in time under the 1D pseudopotential consideration. These oscillations are caused by the reflection of the wave function from the periodical pseudopotential. Due to the ion state occupation oscillations the final occupation is about 0.3 [compare to ~0.05 for the Cu(110) surface]. For the 1D pseudopotential the oscillations do not significantly depend on the ion's parallel velocity. As for the 3D pseudopotential, it also shows oscillations for zero parallel velocity. Note that the oscillation period corresponds to the case of the 1D pseudopotential. But oscillations disappear when parallel velocity becomes significant (>0.1 a.u.). Put in simpler words, due to the electron delay at each moment of time the ion sees a clear surface without a reflected wave function. As a result, the final ion occupation is much smaller, compared to the case of 1D pseudopotential consideration. The above feature is especially significant for modeling of grazing scattering experiments by means of the rate equation. The electron delay effect is noticeable when the ion velocity component parallel

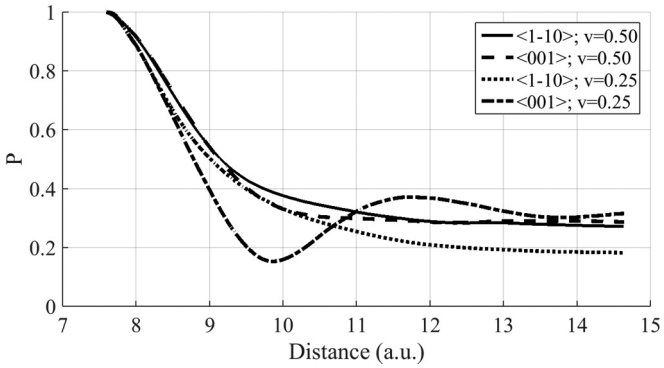

FIG. 9. Influence of ion beam energy and orientation on RCT character. Figure shows H^- ion population dependence on ion-surface distance for different azimuthal angles [close to $\langle 1\bar{1}0\rangle$ and $\langle 001\rangle$ directions in the Cu(110) crystal] and ion velocities ($V_{par} = 0.5$ a.u. vs $V_{par} = 0.25$ a.u.). The H^- ion moves away from the Cu(110) surface with $V_{norm} = 0.02$ a.u.; initial ion-surface distance is 7.6 a.u.

to the surface exceeds the electron propagation speed along that direction. In practice, the typical threshold values of the parallel velocity component are about 0.1–0.2 a.u. for the Cu surface (precise value depends on surface orientation and ion beam lateral direction).

C. Anisotropy of electron propagation and RCT azimuthal dependence

An interesting feature is the anisotropy of electron propagation inside Cu(110). In Fig. 6 one can see that electron propagation along the $\langle 001\rangle$ direction is ~2 times faster than along $\langle 1\bar{1}0\rangle$. Such behavior looks a little bit paradoxical, especially because the interatomic distance along the $\langle 001\rangle$ direction is 3.61 Å, compared to 2.55 Å for $\langle 1\bar{1}0\rangle$. Note that anisotropy of electron propagation does not change significantly for different lateral positions of the H^- ion. Anisotropy is also preserved for different ion-surface distances. The possible explanation of this phenomenon is that electron tunneling from the ion to adjacent atoms acquires a velocity component parallel to the surface. Due to the anisotropy of the Cu(110) surface crystallographic structure the velocity component along the $\langle 001\rangle$ direction is larger than along $\langle 1\bar{1}0\rangle$. This leads to anisotropy of electron propagation. Note that for Cu(100) and Cu(111) surfaces the anisotropy of electron propagation was not observed. The anisotropy of electron propagation is also expected to be found for (110) surfaces of other transition metals, in particular for Ag and Au.

Anisotropy of electron propagation leads to RCT dependence on the ion beam azimuthal angle. Note that this effect has been experimentally registered for H^- scattered from the Cu(110) surface [3,4,30] and Li^0 scattered from Au(110) and Pd(100) surfaces [47]. Figure 9 demonstrates the numerical simulation of H^- population during grazing scattering on Cu(110). We see that as population on time (or distance to the surface) dependence as well as final ion occupations differs for the $\langle 001\rangle$ and $\langle 1\bar{1}0\rangle$ directions. Hereby we can make a conclusion about the numerical observation of the orientation effect, i.e., the influence of the ion beam lateral direction (azimuthal angle) on the final charge state. Also one can see that for large velocity ($V_{par} = 0.5$ a.u.) H^- population

exhibits exponential decay, that commonly corresponds to adiabatic RCT character, while for smaller velocity ($V_{par} = 0.25$ a.u.) the RCT character depends on the ion beam direction: For the $\langle 1\bar{1}0\rangle$ direction the exponential decay takes place, but the H^- population exhibits oscillations for the $\langle 001\rangle$ direction. Such oscillations are typical for the surfaces with a projected band gap, but not for the (110) surface. We think that anisotropy of electron propagation is the reason for such RCT character dependence. For large ion velocity the ion always sees the clean surface (see electron delay effect in Sec. III B); hence the decay is exponential. For smaller velocities, due to anisotropy of electron propagation, the ion sees a clean surface for the $\langle 1\bar{1}0\rangle$ direction and an "occupied" surface for the $\langle 001\rangle$ direction. Hence the RCT exhibits oscillations in the latter case. Note that there is no strict regularity like the "final population along the $\langle 001\rangle$ direction is always lower than along the $\langle 1\bar{1}0\rangle$ direction." Since the final population depends on initial distance and oscillation period, different cases can be realized.

IV. RESULTS OF RCT EXPERIMENTS MODELING

In this section we present results of 3D modeling for a dozen RCT experiments, representing such RCT aspects as (i) different ion types (Li^0 or Li^+ and H^0 or H^-); (ii) different targets (Ag, Al, Au, Cu) and surface electronic structures ("free-electron" for (110) surfaces and projected band gap for (100) or (111) surfaces); (iii) both possible directions of the RCT process (Li^0 ionization vs H^- neutralization); (iv) RCT dependence on ion energy and exit angle. The ion energy in most of the experiments was in the range 0.1–2.5 keV, except in experiments on grazing scattering (up to 25 keV). A significant issue for RCT experiments numerical modeling is Fermi energy (electron work function) value. In our calculations we use the data from Refs. [48–51].

A. RCT dependence on exit angle

In this section we apply a 3D calculation technique to direct modeling of the experiments on RCT 1D or 2D dependence on ion exit angle. Note that due to 3D geometry, such experiments cannot be directly modeled by means of 1D or 2D techniques.

In the first group of experiments [7], a fraction of scattered H^- ions as a function of exit angle was compared for Ag(111) and Ag(110) surfaces. In the original paper the calculation results were presented only for the jellium Ag(110) surface, since the exploited "1D complex angular mode+rate equation" method is not designed for RCT modeling with a projected band gap (excluding the case of cylindrical symmetry). Figure 10 shows 3D calculation results for both surfaces.

The common regularity is that the increase of the H^- fraction with exit angle (measured from the surface) is intuitively reasonable: For larger angles interaction time is shorter and a smaller percentage of electron density has time to tunnel into the target. A more interesting feature is the intersection of H^- fraction curves for Ag(110) and Ag(111) near the angle 15°. For large angles (shorter interaction times) a smaller H^- fraction for Ag(111) is stipulated by a larger electron decay rate. But for small angles (longer interaction time) nonadiabatic effects become significant in the case of Ag(111)—the electron is reflected back due to the projected band gap, and as a result, the effective electron decay rate is smaller compared to Ag(110).

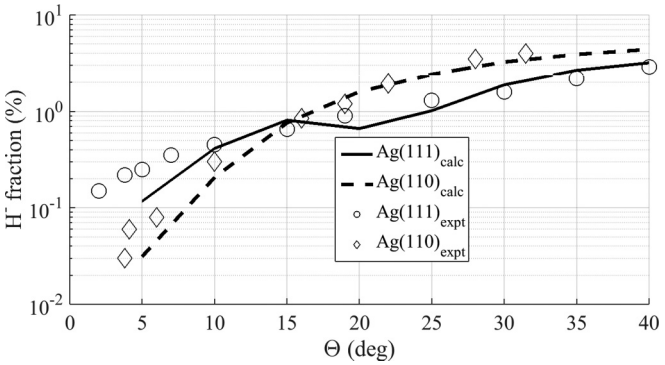

FIG. 10. Comparison of calculation results with experimental data [7]. Figure shows H^- fraction as a function of exit angle. The axes scales are chosen according to the original experimental article. Energy of the primary H^+ ion beam is 1 keV.

One can see that our 3D calculation technique reasonably well reproduces the experimental data and "feels the difference" between adiabatic and nonadiabatic cases. The only fitting parameter, P_0, is equal to 0.09 for both cases. Our calculations significantly underestimate the experimental results in the case of small angles (long interaction times). In order to increase the precision we have to calculate the initial charge state P_0 (to account for ion velocity and ion-surface interaction time), instead of using a constant value. The illustration of P_0 calculation follows.

In Ref. [8] a series of experiments on RCT between hydrogen and polycrystalline Cu is presented. The angular dependence of H^- formation probability was measured for different ion beam energies. Calculations presented in the original article give qualitative correspondence to experimental data.

According to the original paper the dominant surface orientation in polycrystalline Cu is (111), so we model RCT between the hydrogen anion and Cu(111). Figure 11 shows the outer H^- electron in k space for several $H^- - Cu(111)$ distances. One can see that this distribution is rather complex. There are several electron localization points in (k_z, k_ρ) space. For their interpretation it is useful to recall the energy structure of the $H^- - Cu(111)$ system: (i) Surface state energy E_{ss} for Cu(111) is –5.33 eV (measured from vacuum level); (ii) due to pseudocrossing with E_{ss} the ion energy level is split into values ∼–2 and ∼–5 eV; (iii) the conduction band bottom E_b is –12 eV. According to the above energy structure, we interpret the observed electron localization points as follows:

(I) A pair of points (–0.75, 0) and (+0.75, 0) for $z =$ 5 a.u. corresponds to resonant electron transition from the lower ion level (–5 eV) into the surface state. Note that a pair of symmetric points forms something like a standing wave and the electron does not propagate into the metal.

(II) A pair of points (–0.75, 0.5) and (+0.75, 0.5) for $z = 7$ a.u. corresponds to electron transition from the upper ion level (–2 eV) into the surface state. The normal component, 0.75 a.u., corresponds to the energy difference (E_{ss}–E_b), while the lateral component, 0.5 a.u., corresponds to the energy

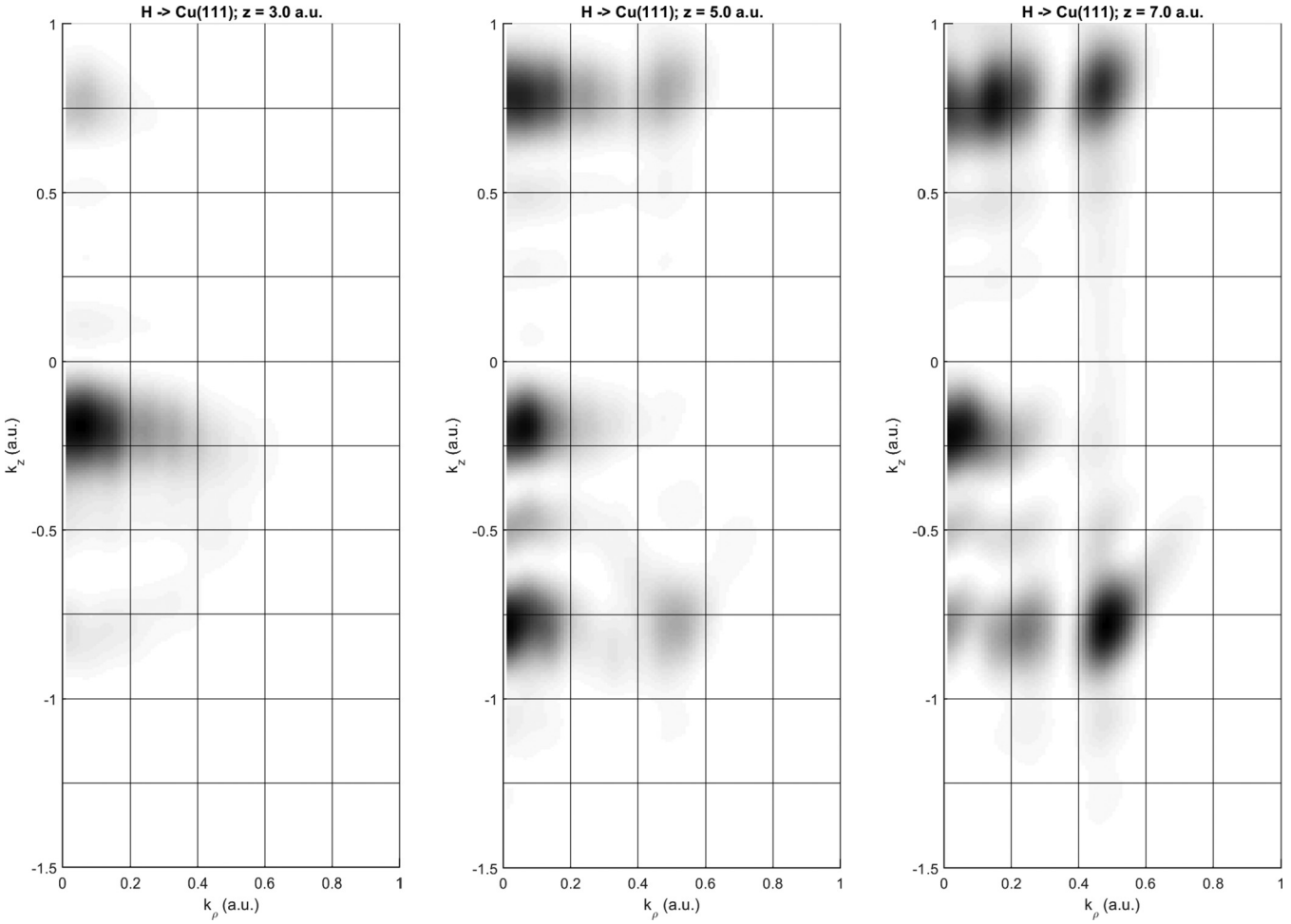

FIG. 11. H^- outer electron density distribution in 2D k space inside the Cu(111) for different ion-surface distances.

difference between the upper energy level and E_{ss}. Like the pair of $(\pm 0.75, 0)$ points, the $(\pm 0.75, 0.5)$ points also form a standing wave along the surface normal, but in this case the electron propagates parallel to the surface.

(III) For larger distances there is a pair of points with coordinates $(\pm 0.75, \sim 0.25)$. We interpret them as intermediate between the (I) and (II) points.

(IV) For all distances a clear structure with coordinates (–0.2, 0) is visible. We suppose that this structure is related to some nonresonant transition, e.g., electron transition from the surface state deep into the metal. Since such transition is considered only for the metal (without the adjacent ion) we exclude this structure from calculation of electron loss or capture weight (see Sec. II D).

Figure 12 illustrates the calculation results and original experimental data. The RCT calculation model in this case is altered to account for the ion velocity for P_0 value calculation: The H^- occupation at a distance z_f is supposed to be proportional to part of the electronic density, located inside the Fermi sphere [see F_{capture} in Eq. (2)]; z_f values for given ion energies and exit angles are in the range 3.6–3.7 a.u.

The P_0 value calculation is significant for quantitative experiment description. Without this modification the H^- fraction values are similar to experimental values, but the $P^-(\Theta = 90^\circ)/P^-(\Theta = 40^\circ)$ ratio is about 1.2 for all energies,

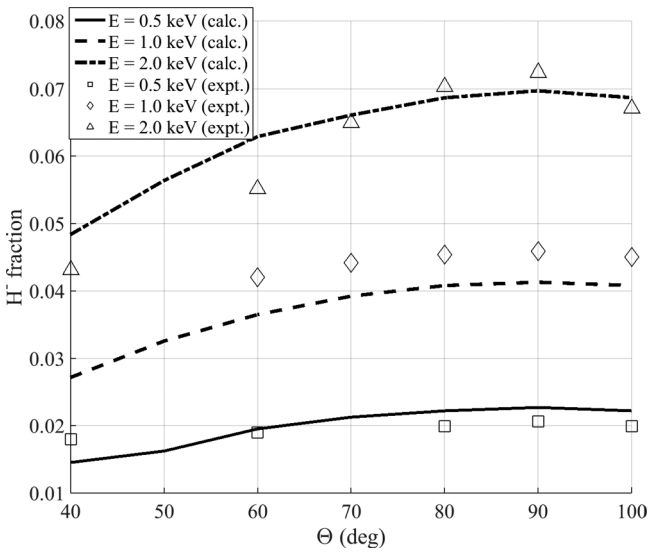

FIG. 12. Comparison of calculation results with experimental data [8]. Figure shows H^- fraction as a function of exit angle for several different energies of the primary ion beam (see legend for details). The axes scales are chosen according to the original experimental article. The incidence angle of the primary H^+ ion beam is 40° to the surface.

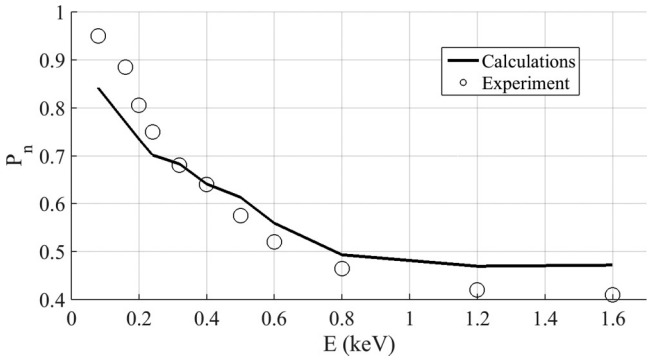

FIG. 13. Comparison of calculation results with experimental data [5]. Figure shows the Li^0 fraction as a function of primary ion beam energy. The incidence angle of the primary Li^+ ion beam is 45° to the surface. Spectra of scattered Li atomic particles (Li^+ and Li^0) are measured along the normal to the surface.

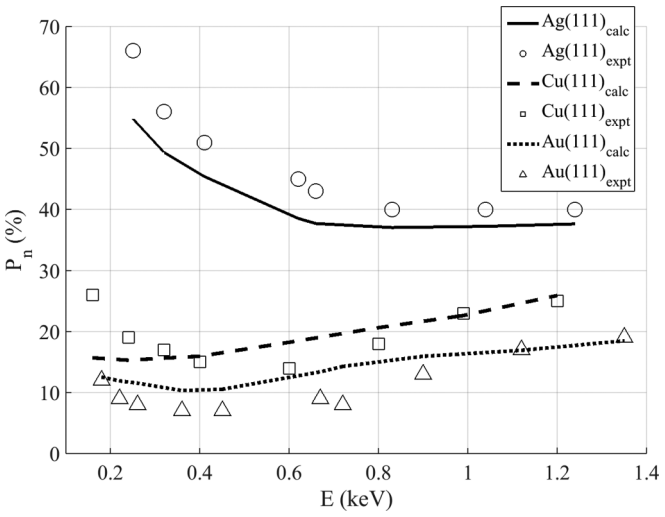

FIG. 14. Comparison of calculation results with experimental data [6]. Figure shows the Li^0 fraction as a function of primary ion beam energy for different surfaces (see legend). The incidence angle of the primary Li^+ ion beam is 45° to the surface. Spectra of scattered Li atomic particles (Li^+ and Li^0) are measured along the normal to the surface.

while in the experiment the H^- fraction practically does not depend on exit angle for low energies (0.5 keV) and changes significantly for higher energies (2 keV). The inclusion of the F_{capture} factor improves the situation:

(I) Due to the frame transformation (see Sec. II D) the F_{capture} factor is affected by ion velocity.

(II) For 0.5 keV the shift in k space is relatively small ($\sim$0.14 a.u.); hence the F_{capture} factor does not change significantly.

(III) For 2 keV the energy shift in k space is about 0.28 a.u.; hence the influence of the exit angle (velocity direction) is stronger.

(IV) for $\Theta = 90^\circ$ velocity is directed along the normal, so the F_{capture} factor increase is larger comparing to $\Theta = 40^\circ$.

Note that our calculations do not reproduce experimentally observed nonmonotonous dependence of ionization probability on ion energy [in the original work $P^-(E = 2\,\text{keV}) > P^-(E = 2.5\,\text{keV})$].

B. RCT dependence on ion energy

The next group of experiments was done by Esaulov and co-workers [5,6]. The fraction of scattered neutral Li^0 atoms was measured as a function of primary Li^+ beam energy. Note that the ionization energy of alkali-metal ions is close to the typical metal work function, hence alkali-metal ions are widely used for surface diagnostics by means of ion beams.

Figure 13 contains the comparison of our calculation results with experimental data [5], for Li interacting with the Ag(100) surface. In the original paper calculation results are also presented that show good quantitative correspondence to experimental data. The common problem for Li^+ neutralization modeling is that neither the 2D wave-packet propagation method, nor the 3D GPU TDSE solver is designed for *ab initio* electron capture calculation.

In the original paper the authors use the time-reversal symmetry assumption, which does not take into account the impact of the ion velocity direction (see Sec. II E for details). The widely used rate equation approach also does not take into account the impact of the ion velocity, since electron capture or loss rates do not depend on the projectiles' velocity. This is a reason why we try to incorporate the influence of ion velocity by the simple suggestion that electron capture by Li^+ and electron loss by Li^0 rates are equal. Hence the "part of electron" captured during Li^+-surface interaction is estimated as the part of electrons lost by Li^0 during the motion along the same trajectory. We assume that Li atoms are completely ionized near the metallic surface ($P_0 = 1$), so our model in this case is parameter free and gives quantitative correspondence to the experiment (Fig. 13). A qualitative description of the Li^0 fraction on energy dependence is rather simple: Interaction time is sufficiently large for small energies, and the Li^+ ion becomes fully neutralized; for larger energies (smaller interaction times) only partial neutralization occurs. Note that despite quantitative correspondence to experimental data, the suggestion of equal electron capture or loss rates for Li could not be automatically applied to other projectiles.

More interesting experimental data [6] are presented in Fig. 14: Unlike Ag(100) and Ag(111) surfaces, the Li^0 fraction during RCT with Cu(111) and Au(111) is a nonmonotone function of ion beam energy (interaction time). In the original paper the calculations only for the jellium Ag surface are presented, and the question of nonmonotone Li^0 fraction dependence remains open.

Our parameter-free calculation model gives quantitative correspondence with the experimental results, including the character of Li^0 fraction dependence on energy and its absolute values for different surfaces. The explanation of nonmonotone Li^0 fraction dependence is based on different Fermi energies and z_f dependence on ion velocity. It is known that the Li^+ ion energy level depends on the ion-surface distance as $E(z_{\text{ion-surface}}) \sim E(\infty) + 1/4z$; more precise dependence is determined numerically (see Sec. II A). The plots of $E(z)$ dependence can be found elsewhere [5]. In the static case for the Ag surface (E_f is about –4.5 eV) z_f is about 6 a.u. In the case of Cu(111) and Au(111) the intersection

distances are about 8–10 a.u., due to the lower Fermi level (–4.94 and –5.31 eV, respectively). For the moving ion its energy level is shifted as $\Delta E(z_{\text{ion-surface}}) = |k'|^2/2 - |k|^2/2 = |v|^2/2 - \vec{v}\cdot\vec{k}$ (see Sec. II D), which leads to z_f dependence on ion velocity. Note that electron density distribution in 3D k space corresponds to the ring (Fig. 4); hence the above formula for the energy shift equation is valid only for ion velocities directed along the normal to the surface. The absolute values of ion energy level shift are about 0.05–0.2 eV and do not depend significantly on the target material, but near the intersection point z_f dependence $E(z)$ changes more rapidly for Ag(100) or Ag(111) than for Cu(111) and Au(111). Therefore to compensate for the same energy level shift fewer z_f changes are necessary in the case of Ag(100) or Ag(111). In our calculation the z_f range was 5.8–6.2 a.u. for Ag(100), 6.5–7.0 a.u. for Ag(111), 7.7–8.4 a.u. for Cu(111), and 7.8–9.1 a.u. for Au(111).

According to the above description, the qualitative explanation of nonmonotone Li^0 fraction dependence is based on a trade-off between influence of interaction time (decreases with energy) and effective RCT rate (increases with energy, due to decrease of z_f). For small ion energies z_f changes are negligible and the Li^+ neutralization probability is defined by interaction time. For larger ion energies z_f is significantly reduced (up to 1 a.u.), which leads to an increase of effective RCT rate and Li^+ neutralization probability.

Note that modeling of nonmonotonous dependence of Li^0 fraction on ion beam energy has been addressed in Refs. [45,47]. Both of those works are based on the rate equation solution and give correspondence to experimental data. The main differences of our approach are (i) we suppose the Li atom to be completely ionized near the surface (in Refs. [45,47] the fraction of Li^0 atoms near the surface is estimated as 40%–100%); (ii) we take into account only electron capture on the outgoing trajectory $z > z_f$ (while integration of he rate equation supposes concurrent electron loss and capture processes). Such significant difference in the initial Li^0 fraction estimation is stipulated by different Li energy level dependences on atom-surface distance. In our approach it increases monotonously with decrease of ion-surface distance and crosses the Fermi level at distances of 6–10 a.u. (see Ref. [5] for details), while in Ref. [45] it is significantly below the Fermi level when Li is located near the surface.

The key advantage of our approach is the subtle accounting of the kinematic factor (shift of electron distribution in k space on the ion velocity value), which leads to z_f dependence on ion beam energy. Our approach gives quantitative correspondence to experimental data [absolute values of neutralization probability and $P(E)$ minima location] for different surfaces; this is a strong argument for the kinematic factor accounting. At the same time, consideration of concurrent electron loss and capture processes could further improve the calculations' precision. Note that due to cylindrical symmetry (the Li^0 atoms are registered along the surface normal), our calculations can be reasonably well reproduced by the 2D wave-packet propagation technique [5,13,16].

C. Grazing scattering and RCT azimuthal dependence

In order to approbate our calculation method for grazing scattering we have modeled the experiment on RCT between hydrogen and the Al(111) surface [11,52]; the results are presented in Fig. 15. Note that for jellium surfaces, our RCT calculation model is very similar to models described in Refs. [3,11,30]. Therefore the calculation results are also similar and very close to experimental data. Let usnote that these are parameter-free calculations.

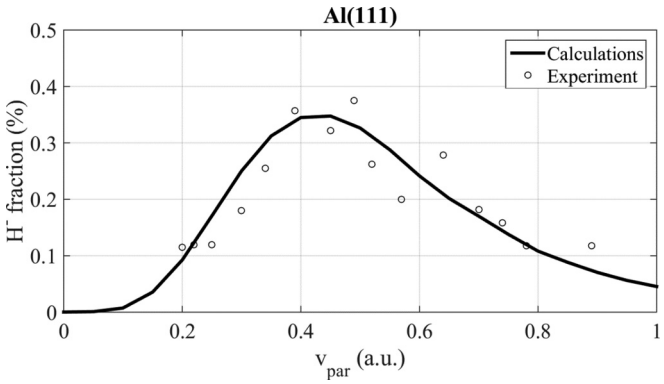

FIG. 15. Comparison of calculation results with experimental data [11,52]. Figure shows a fraction of H^- ions, scattered from Al(111) surface, as a function of the primary ion beam parallel velocity value. The normal velocity of the primary H^+ ion beam is 0.02 a.u.

Figure 16 demonstrates calculation results for a more complicated $H^- - Cu(111)$ interaction. As it was shown in Sec. III A, electron distribution in k space is rather complex in this case. The right part of Fig. 11 ($z = 7$ a.u.) is useful for interpretation of results, because final charge state formation occurs at the distances 6–9 a.u. Note that we exploit structures with coordinates (±0.75, 0.5), (±0.75, 0.25) in (k_z, k_ρ) space, but exclude the structure (–0.2,0) from consideration. These structures form rings in 3D k space. The main peak of the H^- fraction in Fig. 16 (near $v = 0.5$ a.u.) corresponds to the maximal intersection between the main 3D ring (±0.75, 0.5) and the Fermi sphere of the metal. An additional 3D ring (±0.75, 0.25) slightly increases the H^- fraction for velocities around 0.25 a.u. Note that the maximum of the calculated

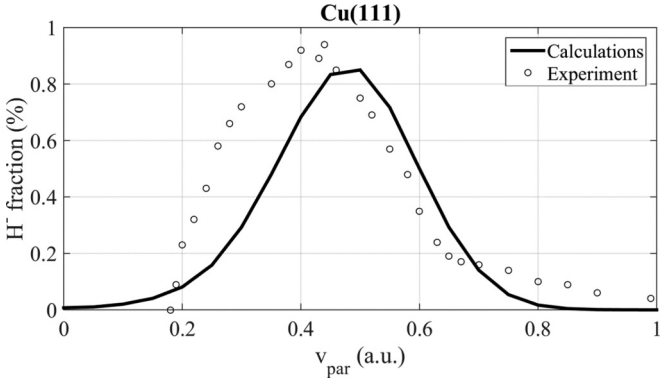

FIG. 16. Comparison of calculation results with experimental data [3,4,30]. Figure shows a fraction of H^- ions, scattered from the Cu(111) surface, as a function of the primary ion beam parallel velocity value. The normal velocity of the primary H^+ ion beam is 0.02 a.u.

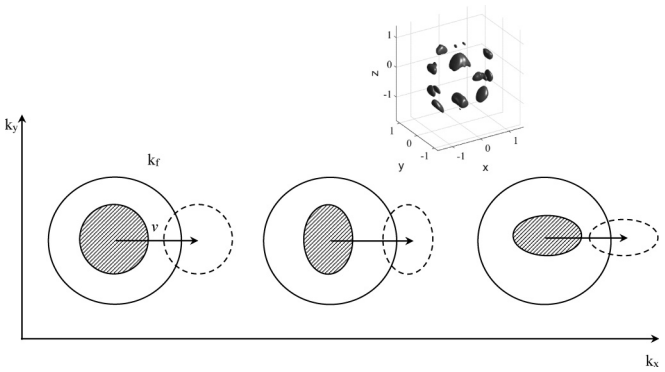

FIG. 17. Illustration of electron propagation anisotropy influence on RCT and H^- fraction azimuthal dependence (details are given in the text). Inset shows H^- outer electron density distribution in 3D k space inside the Cu(110).

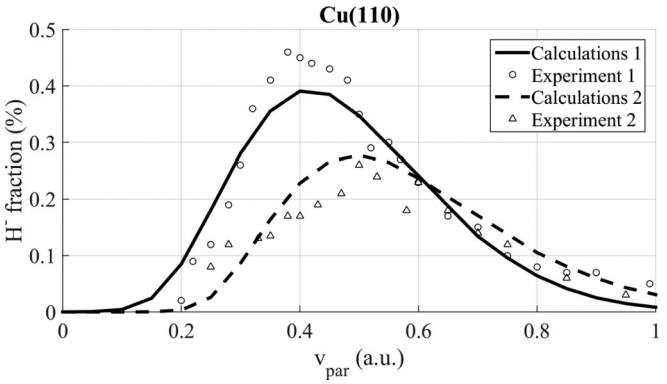

FIG. 18. Comparison of calculation results with experimental data [3,4,30]. Figure shows a fraction of H^- ions, scattered from the Cu(110) surface, for different parallel velocity values of the primary ion beam. The normal velocity of the primary H^+ ion beam is 0.02 a.u. Calculations 1: data for the $\langle 1\bar{1}0\rangle$ azimuthal direction; Calculations 2: data for $\langle 001\rangle$.

$P^-(v)$ dependence is shifted right from the experimental value on ∼0.1 a.u. A possible reason for this is imperfection in the procedure of electron density calculation in k space. For example, we have to calculate electron density not at 100 a.u., but for greater times, when relative weight for the $(\pm 0.75, 0.25)$ ring is larger.

The question of interest is the difference in maximal values of the H^- fraction [∼0.003 for Al(111) and Cu(110) surfaces vs ∼0.009 for the Cu(111) surface]. Such significant difference is related to various $\Gamma_{\text{capture}}/\Gamma_{\text{loss}}$ ratios for these systems. The maximal H^- fraction could be estimated as occupation in the equilibrium point (see Ref. [4] for details): $\frac{dP^-}{dt} = -\Gamma_{\text{loss}} P^-_{\text{eq}} + \Gamma_{\text{capture}}(1 - P^-_{\text{eq}}) = 0$; $P^-_{\text{eq}} = \frac{1}{1+\Gamma_{\text{loss}}/\Gamma_{\text{capture}}} \approx \frac{\Gamma_{\text{capture}}}{\Gamma_{\text{loss}}} = \frac{F_{\text{capture}}}{F_{\text{loss}}}$. The $F_{\text{capture}}/F_{\text{loss}}$ ratio is determined by integration in k space. In the case of jellium metals [Al(111) and Cu(110) surfaces] it is approximately proportional to the intersection between the 3D Fermi spheres of hydrogen and metal, while in the case of a projected gap [Cu(111) surface] it is proportional to the intersection between the 2D Fermi disk of metal and the 2D ring of hydrogen (see Fig. 11). The relative intersection is larger in the last case; hence the $F_{\text{capture}}/F_{\text{loss}}$ ratio and maximal H^- fraction value is larger in the case of Cu(111). It should be noted also that the $F_{\text{capture}}/F_{\text{loss}}$ ratio depends on the ion-surface distance.

In some studies [3,4,30] experimental results are presented demonstrating RCT azimuthal dependence for H^- grazing scattering on the Cu(110) surface. In Sec. III C we addressed this question numerically and observed anisotropy of electron propagation and influence of the azimuthal angle on the RCT rate. According to our model calculations, the maximal difference between the RCT rate along the $\langle 001\rangle$ and $\langle 1\bar{1}0\rangle$ azimuthal directions for Cu(110) is about 10%. This is significantly smaller than the experimentally observed difference. Moreover, the difference in RCT rate does not explain the relative shift of H^- fraction maxima positions.

To understand the reason for the H^- fraction azimuthal dependence let us note that electron propagation in Cu(110) is anisotropic. Figure 17(a) shows electron density distribution in 3D k space. Note that due to the usage of an "atomistic" 3D pseudopotential, this distribution is more complex than in the 2D case and shows density maxima corresponding to different reciprocal lattice vectors (electron transitions to several nearest lattice atoms). The significant feature is the anisotropy of electron density distribution in 3D k space, that has influence on the F_{capture}, F_{loss} factors. The correct F_{capture}, F_{loss} factors' calculation using 3D electron density distribution is the challenge for future studies. In the current research we incorporate anisotropy of electron propagation via modifying the 2D electron density distribution (see Fig. 4). Originally, 2D distribution has cylindrical symmetry around the k_z axis. We artificially break this symmetry by changing the axes scales as $k_x : k_y : k_z = 1.1 : 0.9 : 1.0$ for the $\langle 001\rangle$ direction and $k_x : k_y : k_z = 0.9 : 1.1 : 1.0$ for $\langle 1\bar{1}0\rangle$. Note that in our calculations the ion always moves along the X axis. After such modification the electron density projection in the X-Y plane transforms from a circle to anellipse with approximately the same square.

Figure 17(b) illustrates the F_{capture}, F_{loss} factors' calculation in the case of modified electron density distributions. For the $\langle 1\bar{1}0\rangle$ direction the maximal resonance with the Fermi sphere occurs under the lower velocities, than for the $\langle 001\rangle$ direction. Also for the $\langle 001\rangle$ direction the resonance is wider (greater range of $v_\parallel$).

The second major point is the accounting of the RCT rate anisotropy. To do this, we multiply the RCT rate $\Gamma(z)$ by 1.05 for $\langle 001\rangle$ and 0.95 for the $\langle 1\bar{1}0\rangle$ direction (the relative difference is held at about 10%, estimated from model calculations).

Figure 18 shows that our simple model provides excellent correspondence to experimental data. The surprising fact is that the H^- fraction for the $\langle 1\bar{1}0\rangle$ direction (smaller RCT rate) is larger than the H^- fraction for the $\langle 001\rangle$ direction (greater RCT rate). But this is the consequence of the rate equation solution properties: (i) for greater $\Gamma(z)$ the charge state formation occurs on larger ion-surface distances, $z_c \sim \ln[\alpha\Gamma(z)]$ [4]; (ii) the $F_{\text{capture}}/F_{\text{loss}}$ ratio determines the maximal H^- fraction as a decreasing function of ion-surface distance [at least in the case of $H^- - Cu(110)$ interaction].

Our theoretical description of the RCT azimuthal dependence in grazing scattering experiments provides a clear

logical explanation, while 3D calculations give numerical correspondence to experimental results.

V. CONCLUSIONS

We have developed the technique of RCT modeling between an atomic particle and a metal surface, which accounts for the realistic (atomic scale) structure of the surface. The developed technique is based on the direct 3D TDSE solution for one active electron, moving in the pseudopotential formed by an ionic core and a metal surface. The key point is the usage of 3D pseudopotentials, which describes the metal structure on the atomic level. Three-dimensional pseudopotentials for Cu(100), Cu(110), and Cu(111) surfaces have been calculated by means of DFT, considering the known Cu crystallographic structure. The obtained 3D pseudopotentials reproduce the major RCT features. In particular, in the case of jellium surfaces (110) we observe the electron tunneling along the surface normal and its unrestricted propagation deep into the metal. For the surfaces with a projected band gap (100), (111), the electron motion along the surface normal is restricted. The dependence of the RCT rate (level width) on ion-surface distance obtained for the 3D pseudopotential corresponds to the RCT rate obtained by means of well-known effective 1D pseudopotentials. Also the presented 3D pseudopotential for Cu(111) satisfactorily reproduce the energy of the surface state.

The developed technique has been applied to several model problems in order to investigate the RCT features, arising from a realistic (3D) surface description. Several effects were revealed, that should be taken into account during RCT experiments modeling.

In the fixed-ion problem the ion's lateral position was found to have a small influence on the RCT rate and character. The RCT is "averaged" due to the interaction with several neighbor surface atoms. For the dynamical problems (nongrazing angles) the RCT was found to be dependent mainly on the distance of the closest approach and velocity of the ion. The ions' velocity orientation along the crystallographic axis as well as the lateral shift of trajectory do not influence significantly the final charge state of the ion. In this sense the usage of 3D pseudopotentials does not give great benefits compared to well-known 1D pseudopotentials.

The difference between usage of 3D and 1D pseudopotentials becomes significant for the grazing ions' trajectories, when the normal velocity component is small. In the case of the 1D pseudopotential (which is constant in the XY plane) the electron tunneled into the metals preserves the lateral velocity component, but for the real 3D pseudopotential the electron movement parallel to the surface is limited due to the pseudopotential periodicity. Therefore the electron in the metal is delayed relative to the moving ion. This fact has a very interesting consequence for the surfaces with a projected band gap. Under the 1D pseudopotential consideration the charge state of the ion (population) oscillates in time due to the reflection of the wave function from the periodical pseudopotential. These population oscillations disappear under 3D pseudopotential consideration of grazing scattering. Put in simpler words, due to the electron delay at each moment of time the ion sees a clear surface without a reflected wave function.

Another interesting 3D effect is anisotropy of the electron propagation relative to the surface lattice. For example, for the Cu(110) surface the electron propagation speed along the $\langle 001\rangle$ direction is $\sim$2 times larger than along the $\langle 1\bar{1}0\rangle$ direction. Note that this effect was not observed for Cu(100) and Cu(111) surfaces. The full 3D modeling enables us to reveal RCT azimuthal dependence, when the RCT rate and the final ion occupation depend on the ion velocity orientation relative to the surface directions of dense and sparse atomic packing. Also, we have found that during grazing scattering the RCT character (adiabatic or nonadiabatic) depends not only on interaction time and surface structure, but also on the parallel velocity value and ion beam orientation.

Further we have developed a theoretical basic and calculation methodology for three-dimensional RCT modeling and successfully applied them to a variety of experimental data. The core of the calculation methodology is a combination of a 3D TDSE solver with 3D pseudopotentials, derived from *ab initio* DFT calculations. Such combination provides *ab initio* RCT modeling on an atomic level.

The key point of our approach to the RCT calculation is determination of the energetically allowed electron transfer direction (electron loss or electron capture). We perform RCT direction analysis in k space and apply Galilean transformation between frames of a moving projectile and a still target. In the case of small velocities and simple electron distribution in k space our approach consists in correct determination of intersection distance between the energy level of the ion and the Fermi energy; after that we directly solve the TDSE on the outgoing trajectory. In the case of grazing scattering, we account for concurrent processes of electron capture and loss via solving the rate equation. Note that in the case of grazing scattering the rate equation (adiabatic approximation) is applicable even to RCT with projected band-gap surfaces due to the so-called electron delay effect. It should be stressed that our model includes only one fitting parameter and is parameter free in the important cases of RCT with alkali-metal atoms and grazing scattering.

We have considered a dozen RCT experiments, representing such RCT aspects as (i) different ion types ($Li^0/Li^+$and H^0/H^-); (ii) different targets (Ag, Al, Au, Cu) and surface electronic structures [free-electron for (110) surfaces and projected band gap for (100) or (111) surfaces]; (iii) both possible directions of the RCT process (Li^0 ionization vs H^- neutralization); (iv) RCT dependence on ion energy and exit angle. The ion energy in most of the experiments was in the range 0.1–2.5 keV, except in experiments on grazing scattering (up to 25 keV).

In most cases our approach provides quantitative correspondence with available experimental data. Note that some of these experiments have not been modeled before due to the absence of 3D simulation techniques. Among the presented simulations of experimental data we should emphasize (i) explanation of nonmonotonous dependence of Li^0 fraction on ion beam energy during scattering on Au(111) and Cu(111) surfaces; (ii) quantitative modeling of H^- fraction azimuthal dependence for hydrogen grazing scattering on Cu(110).

Finally, we should mention that the presented technique of 3D RCT modeling is not the only one possible. For example, the group of Thumm (Kansas State University, USA) has presented several studies where 3D RCT was incorporated into the Anderson-Newns model. The benefit of our approach is *ab initio* direct modeling of electron loss by the ion, which directly takes into account the ion's movement (nonadiabatic effects) and allows exploring the electron distribution inside the surface. On the other hand, our approach is not designed for direct modeling of electron capture by the ion, and some additional assumptions should be used to model this branch of RCT.

ACKNOWLEDGMENTS

The author gratefully acknowledges the financial support provided by the Russian Foundation for Basic Research (Grant No. 16-02-00478). The parallel computing facilities were provided by MV Lomonosov Moscow State University.

[1] R. Brako and D. M. Newns, Rep. Prog. Phys. **52**, 655 (1989).
[2] H. Shao, D. C. Langreth, and P. Nordlander, in *Low Energy Ion-Surface Interactions*, edited by J. W. Rabalais (Wiley, New York, 1994).
[3] T. Hecht, H. Winter, A. G. Borisov, J. P. Gauyacq, and A. K. Kazansky, Phys. Rev. Lett. **84**, 2517 (2000).
[4] H. Winter, Phys. Rep. **367**, 387 (2002).
[5] A. R. Canario, A. G. Borisov, J. P Gauyacq, and V. A. Esaulov, Phys. Rev. B **71**, 121401(R) (2005).
[6] A. R. Canario, T. Kravchuk, and V. A. Esaulov, New J. Phys. **8**, 227 (2006).
[7] L. Guillemot and V. A. Esaulov, Phys. Rev. Lett. **82**, 4552 (1999).
[8] B. Bahrim, B. Makarenko, and J. W. Rabalais, Surf. Sci. **594**, 62 (2005).
[9] M. Maazouz, A. G. Borisov, V. A. Esaulov, J. P. Gauyacq, L. Guillemot, S. Lacombe, and D. Teillet-Billy, Phys. Rev. B **55**, 13869 (1997).
[10] J. N. M. Van Wunnik, R. Brako, K. Makoshi, and D. M. Newns, Surf. Sci. **126**, 618 (1983).
[11] A. G. Borisov, D. Teillet-Billy, and J. P. Gauyacq, Phys. Rev. Lett. **68**, 2842 (1992).
[12] A. G. Borisov, D. Teillet-Billy, J. P. Gauyacq, H. Winter, and G. Dierkes, Phys. Rev. B **54**, 17166 (1996).
[13] A. A. Magunov, D. K. Shestakov, I. K. Gainullin, and I. F. Urazgildin, J. Surf. Invest. X-Ray, Synchrotron Neutron. Tech. **2**, 764 (2008).
[14] D. K. Shestakov, T. Yu. Polivnikova, I. K. Gainullin, and I. F. Urazgildin, Nucl. Instrum. Methods Phys. Res., Sect. B **267**, 2596 (2009).
[15] A. R. Canario and V. A. Esaulov, J. Chem. Phys. **124**, 224710 (2006).
[16] I. K. Gainullin and I. F. Urazgildin, Izv. RAN, Ser. Fiz. **70**, 897 (2006) [Bull. Russ. Acad. Sci.: Phys. **70**, 1024 (2006)].
[17] I. K. Gainullin, E. Yu. Usman, and I. F. Urazgildin, Nucl. Instrum. Methods Phys. Res., Sect. B **232**, 22 (2005).
[18] I. K. Gainullin, E. Yu. Usman, Y. W. Song, and I. F. Urazgil'din, Vacuum **72**, 263 (2004).
[19] E. R. Amanbaev, I. K. Gainullin, E. K. Zykova, and I. F. Urazgildin, Thin Solid Films **519**, 4737 (2011).
[20] E. Yu. Zykova, A. A. Khaidarov, I. P. Ivanenko, and I. K. Gainullin, J. Surf. Invest. X-Ray, Synchrotron Neutron Tech. **6**, 877 (2012).
[21] I. K. Gainullin and I. F. Urazgildin, Phys. Rev. B **74**, 205403 (2006).
[22] I. K. Gainullin and M. A. Sonkin, Phys. Rev. A **92**, 022710 (2015).
[23] M. Taylor and P. Nordlander, Phys. Rev. B **64**, 115422 (2001).
[24] H. Chakraborty, T. Niederhausen, and U. Thumm, Phys. Rev. A. **69**, 052901 (2004).
[25] J. Sjakste, A. G. Borisov, and J. P. Gauyacq, Nucl. Instrum. Methods Phys. Res., Sect. B **203**, 49 (2003).
[26] B. Bahrim, S.Yu, B. Makarenko, and J.W. Rabalais, Surf. Sci. **603**, 703 (2009).
[27] B. Obreshkov and U. Thumm, Phys. Rev. A **74**, 012901 (2006).
[28] B. Obreshkov and U. Thumm, Phys. Rev. A **83**, 062902 (2011).
[29] B. Obreshkov and U. Thumm, Phys. Rev. A **87**, 022903 (2013).
[30] T. Hetch, H. Winter, A. G. Borisov, J. P. Gauyacq, and A. K. Kazansky, Faraday Discuss. **117**, 27 (2000).
[31] I. K. Gainullin and M. A. Sonkin, Comput. Phys. Commun. **188**, 68 (2015).
[32] I. K. Gainullin, Comput. Phys. Commun. **210**, 72 (2017).
[33] E. Yu. Usman, I. F. Urazgil'din, A. G. Borisov, and J. P. Gauyacq, Phys. Rev. B **64**, 205405 (2001).
[34] J. Burgdorfer, in *Review of Fundamental Processes and Applications of Atoms and Ions*, edited by C. D. Lin (World Scientific, Singapore, 1993).
[35] P. J. Jennings, R. O. Jones, and M. Weinert, Phys. Rev. B **37**, 6113 (1988).
[36] E. V. Chulkov, V. M. Silkin, and P. M. Echenique, Surf. Sci. **437**, 330 (1999).
[37] S. S. Tsirkin, S. V. Eremeev, and E. V. Chulkov, Fiz. Tverd. Tela **52**, 175 (2010) (in Russian).
[38] U. Thumm, https://jrm.phys.ksu.edu/Research/Meetings/DOE-AMOP/ut.pdf.
[39] J. S. Cohen and G. Fiorentini, Phys. Rev. A **33**, 1590 (1986).
[40] J. N. Bardsley, Case Stud. At. Phys. **4**, 299 (1974).
[41] V. A. Ermoshin and A. K. Kazansky, Phys. Lett. A **218**, 99 (1996).
[42] P. Giannozzi, S. Baroni, N. Bonini, M. Calandra, R. Car, C. Cavazzoni, D. Ceresoli, G. L. Chiarotti, M. Cococcioni, I. Dabo, A. Dal Corso, S. Fabris, G. Fratesi, S. de Gironcoli, R. Gebauer, U. Gerstmann, C. Gougoussis, A. Kokalj, M. Lazzeri, L. Martin-Samos *et al.*, J. Phys.: Condens. Matter, **21**, 395502 (2009).
[43] https://www.vasp.at/; G. Kresse and J. Hafner, Phys. Rev. B **47**, 558 (1993).
[44] A. G. Borisov, A. K. Kazansky, and J. P. Gauyacq, Phys. Rev. B **59**, 10935 (1999).
[45] C. Meyer, F. Bonetto, R. Vidal, E. A. Garcia, C. Gonzalez, J. Ferron, and E. C. Goldberg, Phys. Rev. A **86**, 032901 (2012).

[46] J. Merino, N. Lorente, M.Yu. Gusev, F. Flores, M. Maazouz, L. Guillemot, and V. A. Esaulov, Phys. Rev. B **57**, 1947 (1998).
[47] L. Chen, J. Shen, J. Jia, T. Kandasamy, K. Bobrov, L. Guillemot, J. D. Fuhr, M. L. Martiarena, and V. A. Esaulov, Phys. Rev. A **84**, 052901 (2011).
[48] J. Holzl and F. K. Schulte, *Work Functions of Metals in Solid Surface Physics*, edited by G. Hohler (Springer-Verlag, Berlin, 1979).
[49] J. C. Riviere, *Work Function: Measurements and Results, in Solid State Surface Science, Vol. 1*, edited by M. Green (Decker, New York, 1969).
[50] H. B. Michaelson, J. Appl. Phys. **48**, 4729 (1977).
[51] https://public.wsu.edu/∼pchemlab/documents/Work-functionvalues.pdf.
[52] F. Wyputta, R. Zimny, and H. Winter, Nucl. Instrum. Methods Phys. Res., Sect. B **58**, 379 (1991).